

IRIS: Inverse Rendering of Indoor Scenes from Low Dynamic Range Images

Chih-Hao Lin^{1,2} Jia-Bin Huang^{1,3} Zhengqin Li¹ Zhao Dong¹ Christian Richardt¹
 Tuotuo Li¹ Michael Zollhöfer¹ Johannes Kopf¹ Shenlong Wang² Changil Kim¹

¹Meta ²University of Illinois Urbana-Champaign ³University of Maryland College Park

<https://irisldr.github.io/>

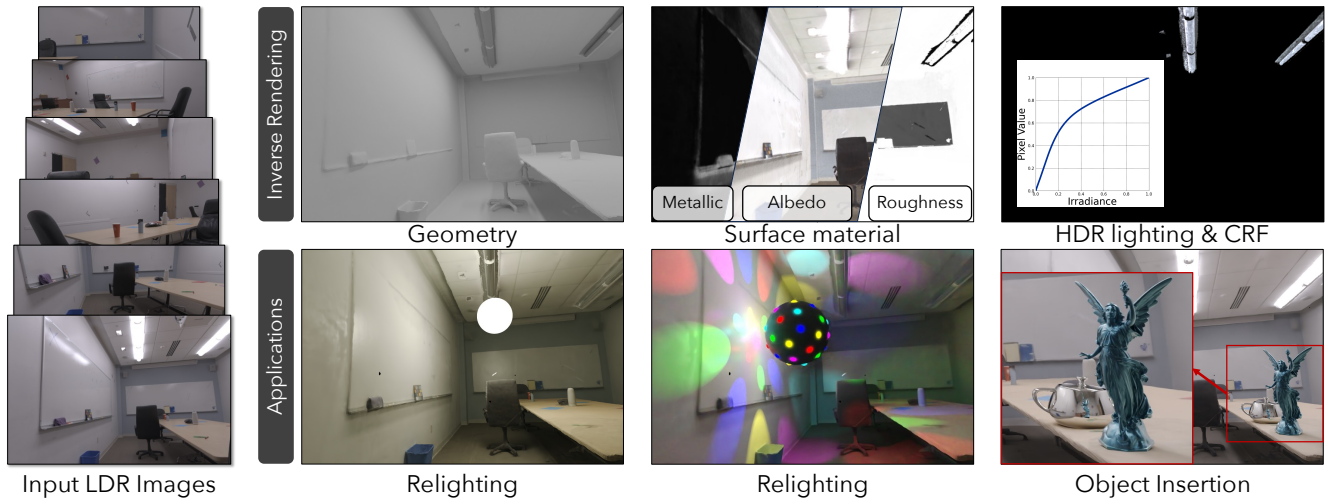


Figure 1. **Physically-based inverse rendering from LDR images.** Our method takes LDR input images and estimates high-quality spatially-varying HDR lighting, physically-based material properties, and a camera response function (CRF). This decomposition allows us to insert objects or new light sources, and to relight the scene in a physically accurate manner.

Abstract

Inverse rendering seeks to recover 3D geometry, surface material, and lighting from captured images, enabling advanced applications such as novel-view synthesis, relighting, and virtual object insertion. However, most existing techniques rely on high dynamic range (HDR) images as input, limiting accessibility for general users. In response, we introduce IRIS, an inverse rendering framework that recovers the physically based material, spatially-varying HDR lighting, and camera response functions from multi-view, low-dynamic-range (LDR) images. By eliminating the dependence on HDR input, we make inverse rendering technology more accessible. We evaluate our approach on real-world and synthetic scenes and compare it with state-of-the-art methods. Our results show that IRIS effectively recovers HDR lighting, accurate material, and plausible camera response functions, supporting photorealistic relighting and object insertion.

1. Introduction

Physically based inverse rendering enables reconstructing realistic material properties and lighting in scenes. This decomposition is valuable for various applications, including relighting, material editing, and realistic object insertion. However, most existing inverse rendering methods require input images with high dynamic range (HDR) to capture the full light transport in the scene. This poses a significant barrier to broader adoption, as HDR capture typically requires specialized hardware or merging multiple aligned LDR images through exposure bracketing [35].

Most common imaging sensors do not capture sufficient dynamic range for scenes’ light-emitting and dark regions. Moreover, cameras often convert raw sensor readings to 8-bit low-dynamic-range (LDR) images for storage and transmission. The non-linear mapping and quantization lead to the additional loss of lighting information. The complex light transport in indoor environments makes reconstructing the original HDR lighting – critical for faithful inverse rendering – even more challenging. If material and lighting estimation

could be achieved from a “casual” capture using standard devices like cameras or phones, inverse rendering would become far more accessible to a wider range of users.

Many state-of-the-art inverse rendering methods rely on HDR inputs to accurately recover material properties and lighting [44, 49, 53]. Some approaches attempt to overcome this issue by taking LDR images as inputs and solving for the lighting. However, these methods often make simplifying assumptions, such as infinitely distant light sources [42], requiring additional inputs like emitter masks [56], or neglecting multi-bounce light transport [46, 53, 56]. As a result, these methods struggle to handle the complex light transport in indoor scenes and often fail to produce high-quality surface material and lighting.

To address these challenges, we introduce IRIS, an inverse rendering method for indoor scenes, using only multi-view LDR images. IRIS models tone mapping (i.e., HDR-to-LDR conversion), allowing us to work directly with LDR inputs. IRIS automatically identifies emitters and reconstructs spatially varying HDR lighting through physically based inverse rendering, which is crucial for faithful material estimation. Jointly estimating lighting, surface material, and camera response function (CRF) leads to unstable optimization due to ambiguities. To tackle this, we design a novel optimization strategy that effectively resolves these ambiguities, enabling high-quality estimation. Our core contributions are:

1. IRIS faithfully estimates spatially-varying HDR lighting, physically-based materials, and camera response function from LDR images and outperforms several state-of-the-art inverse rendering methods.
2. We explicitly model LDR image formation in our (inverse) rendering pipeline so that LDR images can be used directly, broadening the accessibility of high-quality inverse rendering.
3. Finally, IRIS is extensively evaluated on synthetic and real-world scenes, demonstrating diverse and realistic view synthesis, relighting, and object insertion.

2. Related Work

Data-driven inverse rendering. Inverse rendering seeks to reconstruct a scene’s geometry, material, and lighting from single or multiple images. This process is notoriously challenging and ill-posed due to the inherent ambiguity. Numerous methods employ deep priors learned from large-scale datasets for different tasks, including intrinsic image decomposition [20, 21], SVBRDF estimation [6, 19, 22, 51, 57], lighting estimation [8, 23, 38], lighting editing [25] and relighting [34]. These learning-based methods take a single or a few images [2, 38] as inputs, reducing capturing requirements of classical measurement-based methods [9]. However, high-quality datasets are essential for data-driven methods to achieve compelling generalization ability. Synthetic

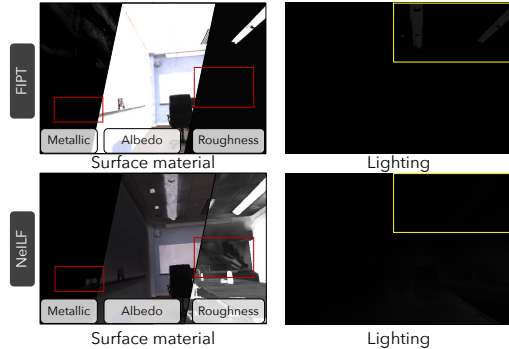


Figure 2. **Limitation of SOTA.** A typical image formation process causes the loss of lighting information, posing challenges in inverse rendering. FIPT [44] assumes HDR input and NeILF [46] ignores multi-bounce light transport. Both methods fail to estimate accurate material (red boxes) and HDR lighting (yellow boxes). We demonstrate significantly better results (Figure 1).

datasets are often used for training because ground-truth labeling is challenging to obtain in real environments. Despite efforts to create photorealistic synthetic datasets [20, 24, 36], the inherent diversity of real-world environments, especially in complex indoor scenes, still causes a substantial domain gap. Furthermore, these methods do not reconstruct complete 3D scenes and fail to render consistent novel views under novel illuminations. Our method utilizes prediction from a data-driven method [57] for initialization and reconstructs 3D geometry, material and lighting with a carefully designed optimization framework, demonstrating superior performance for real-world scenes.

Optimization-based inverse rendering. Differentiable path tracing [14] enables the direct optimization of scene parameters with physically-based multi-bounce light transport. Recent methods, including MILO [49], IPT [1], and follow-up work [33] exploit this to jointly optimize BRDF and lighting emission, accounting for global light transport. FIPT [44] utilizes a factored light transport formulation for BRDF estimation and emitter detection. Nevertheless, these methods assume piecewise constant materials or are designed to take high-dynamic range images as input, and the robustness is limited in real-world scenes. Several recent NeRF-based approaches [12, 15, 26, 32, 40, 42, 54, 55] parameterize materials as a neural field and optimize with a volume rendering formulation. They tend to assume distant lighting and cannot handle spatially varying lighting in indoor environments well. NeILF [46] and NeILF++ [53] represent spatially-varying lighting as a neural field, I²-SDF [56] constructs lighting from given emitter masks. While handling more complex lighting, these works require additional assumptions (e.g., HDR input, emitter masks), and single-bounce ray tracing cannot model complex light transport. In contrast, our method automatically identifies emitters and reconstructs HDR lighting from casual (LDR) images, while achieving high-quality material and lighting estimation that

outperforms prior work in this practical scenario.

CRF and HDR estimation. The complete information about the illumination is usually lost within the photography pipeline. Estimating the HDR lighting and CRF enables us to edit photos and achieve realistic object insertion. Debevec and Malik [5] propose to take multiple photos with varying exposure levels to recover the CRF and HDR image. Some previous works [27, 28, 45, 52] predict HDR images with a data-driven approach by learning the LDR–HDR mapping from a single image. However, these methods rely on HDR data for training, and the estimation is inconsistent across views and scenes. To handle the HDR–LDR mapping, FIPT [44] and RawNeRF [30] assume a known gamma correction function; NeILF++ [53] learn a single gamma correction parameter; HDR-NeRF [13] parameterizes tone-mapping function with an MLP. However, these works are designed to take HDR images or LDR with multiple exposure levels as input. We leverage physically-based rendering to recover spatially varying BRDF, HDR illumination, and CRF from LDR images. Our method generates realistic view synthesis, relighting, and object insertion.

3. Background: LDR image formation

Real-world radiance exhibits high dynamic range (HDR) and contains bright light sources and dark regions. To preserve the complete lighting information, HDR images are typically produced with a high-end camera, laborious exposure bracketing [5], and are stored in specialized format (16 or 32 bits per color channel). However, capturing HDR is often impractical for casual users and is typically absent in standard photography assets. Due to the limitations of standard sensors and displays, the radiance is frequently processed with multiple stages to produce low dynamic range (LDR) images stored in more lightweight formats (such as JPEG or PNG at 8 bits and RAW at 12 bits per color channel). We describe the major steps in this process below.

Dynamic range clipping. Given the scene irradiance E and exposure time Δt , the observed radiance is clipped at a certain maximum value due to the sensor limitation, which could be formulated as: $Z_c = \min(E\Delta t, 1)$. Due to the clipping operation, the lighting information is lost for over-exposed/saturated pixels.

Non-linear mapping of CRF. To enhance the image’s visual quality and match the human perception of the scene, the clipped intensity is further transformed with a non-linear camera response function (CRF) to produce LDR pixel values: $Z = \text{CRF}(Z_c) = \text{CRF}(\min(E\Delta t, 1))$. Please refer to Debevec and Malik [5] for a more detailed imaging pipeline explanation.

Challenges in inverse rendering; Real-world scenes often exhibit extreme variances in radiance, making it challenging to capture these scenes in LDR images without under-

exposing or saturating them. Due to the clipping and non-linear CRF mapping, critical lighting information is lost, posing challenges in previous works, illustrated in Figure 2. In this work, we propose an inverse rendering framework that jointly recovers HDR lighting and CRF from LDR images.

4. Representation and rendering

Camera response function (CRF). The CRF is crucial for recovering original radiance from 8-bit LDR images. However, the CRF varies with each camera and is often unknown to users. Thus, deducing the CRF from LDR image observations is critical to our solution. We use Gross et al.’s [11] empirical model of response (EMoR) for CRF modeling [27]. They collected a database of 201 real-world CRFs of various devices and parameterized them as vectors. A mean curve $\bar{\mathbf{g}}$ and PCA basis \mathbf{g}_b are calculated from the database, and we parameterize a learnable CRF as

$$\mathbf{g} = \bar{\mathbf{g}} + \Sigma w \mathbf{g}_b, \mathbf{g} \in \mathbb{R}^{1024}, \quad (1)$$

where $\{w\}$ weigh each basis curve and are learnable parameters. The non-linear function is discretized as $\text{CRF}(x) = \text{LERP}(\{g_k\}_k, x)$, which linearly interpolates the uniformly sampled CRF $\{g_k\}_{k=0}^{1023} \in [0, 1]^{1024}$, independently per color channel. We make this design choice because it covers most of the CRF spaces, and the simplicity makes it easy to enforce regularization, which brings huge advantage in the complex optimization of inverse rendering.

Spatially-varying lighting. While environment maps handle object-centric and outdoor scenes well [15, 39, 42, 54], they cannot capture complex spatially-varying lighting of indoor scenes. To handle this, we define direct lighting on the scene mesh and measure emission as view-independent radiance: $\mathbf{L}_e(\mathbf{x}) \in \mathbb{R}^3$. The parameterization of $\mathbf{L}_e(\mathbf{x})$ is detailed in our supplementary material. We also define an emitter mask $M_e(\mathbf{x}) \in \{0, 1\}$ to denote whether a surface point \mathbf{x} is on an emitter. Global illumination is represented as a view-independent surface light field (SLF): $\mathbf{L}_{\text{SLF}}(\mathbf{x}) \in \mathbb{R}^3$. The sRGB pixel colors of input LDR images are linearized with an inverse CRF mapping: $\mathbf{I}_{\text{linear}} = \text{CRF}^{-1}(\mathbf{I}_{\text{LDR}})$. If a voxel contains no surface, it is set to zero; otherwise, it collects the average linearized radiances across all input images with ray casting. This greatly accelerates the approximation of global illumination without requiring multi-bounce ray tracing.

Material BRDF. We represent spatially-varying materials using the Cook-Torrance BRDF [4]. The surface albedo $\mathbf{a}(\mathbf{x}) \in \mathbb{R}^3$, roughness $\sigma(\mathbf{x}) \in \mathbb{R}$, and metallicity $m(\mathbf{x}) \in \mathbb{R}$ model the diffuse reflectance $\mathbf{k}_d = \mathbf{a} \cdot (1 - m)$ and specular reflectance $\mathbf{k}_s = 0.04 \cdot (1 - m)$, and are parameterized as a neural field $\mathbf{f}: \mathbf{x} \mapsto (\mathbf{a}, \sigma, m)$, implemented with multi-resolution hash encoding and an MLP [31].

Factorized light transport. To render images from scene geometry, material, and lighting information, We follow

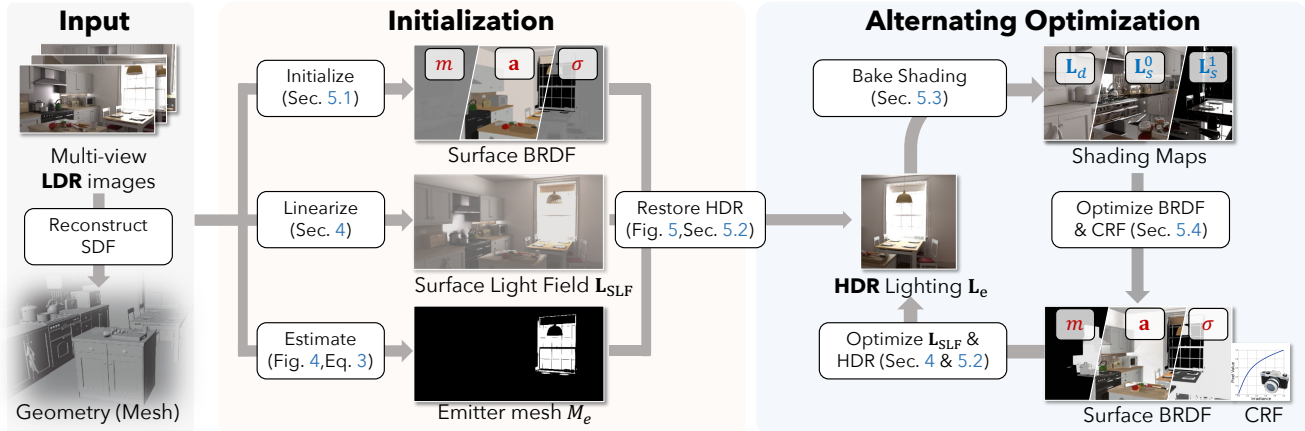


Figure 3. **Framework Overview.** Given multi-view posed LDR images and a surface mesh, our inverse rendering pipeline is divided into two main stages. In the initialization stage, we initialize the BRDF (Section 5.1), extract a surface light field (Section 4), and estimate emitter geometry (Equation (3)). In the optimization stage, we first recover HDR radiance from the LDR input (Section 5.2), then bake shading maps (Section 5.3), and jointly optimize BRDF and CRF parameters (Section 5.4). The improved parameters are used to refine the emission again. These three steps are repeated until convergence.

the rendering equation [16] to model physically-based light transport for realistic rendering:

$$\mathbf{L}_o(\mathbf{x}, \omega_o) = \mathbf{L}_e(\mathbf{x}, \omega_o) + \int_{\Omega^+} \mathbf{L}_i(\mathbf{x}, \omega_i) f(\mathbf{x}, \omega_i, \omega_o) d\omega_i, \quad (2)$$

where \mathbf{L}_o is the radiance observed along a ray at a 3D position \mathbf{x} in direction ω_o , \mathbf{L}_e is the emission term, $\mathbf{L}_r = \int_{\Omega^+} \mathbf{L}_i(\mathbf{x}, \omega_i) f(\mathbf{x}, \omega_i, \omega_o) d\omega_i$ is the reflectance term, and $f(\mathbf{x}, \omega_i, \omega_o)$ is the BRDF. The recursive nature of the rendering equation is approximated with Monte-Carlo path tracing [16, 18]. However, modeling multiple bounces is still computationally expensive and unstable in the inverse rendering process. To enhance the efficiency and robustness of the optimization, we follow FIPT [44] and adopt factorized light transport [17, 37, 41], which precomputes shading maps $\mathbf{L}_d, \mathbf{L}_s^0, \mathbf{L}_s^1$ and linearly interpolates with roughness to obtain final rendering. Detailed notation and formulation are available in supplementary material.

5. Inverse Rendering from LDR Images

Given multi-view posed LDR images $\{\mathbf{I}_i\}$ captured with the same or varying exposure levels $\{\Delta t_i\}$, our goal is to estimate spatially-varying HDR lighting, surface material (as albedo, roughness, and metallic), and the camera response function (CRF) shared by all input images. We assume that the primary light sources are observed in the input images, following the recent literature [44, 49, 56].

Previous approaches perform differentiable path tracing during the material and lighting optimization [1, 33], but the number of samples is limited due to heavy computation. This introduces high variance and unstable estimation. The factorized formulation [17, 37, 41, 44] splits light transport into BRDF parameters and shading, and enables updating

them alternately. While the method is shown to be more stable and produce high-quality decompositions, it requires HDR images as input to aggregate and bake shading maps, detect emitters, and estimate HDR emissions.

To address this ill-posed optimization problem, we propose a multi-stage optimization strategy alternately estimating spatially varying lighting, material, and CRF. Specifically, we (1) initialize the BRDF with an off-the-shelf monocular inverse rendering method (Section 5.1), (2) recover HDR lighting from LDR with physically-based rendering (Section 5.2), (3) bake the diffuse and specular shading (Section 5.3), and (4) jointly estimate BRDF and CRF (Section 5.4). We repeat Steps 2–4 in that order until all estimates are converged. Figure 3 illustrates our framework.

Geometry reconstruction. From input images with camera poses, we reconstruct the geometry with BakedSDF [47], and use normal estimation from off-the-shelf method [7] for regulating surface geometry, following MonoSDF [50].

5.1. BRDF Initialization

For each input image \mathbf{I}_i , we predict a 2D albedo map \mathbf{A}_i using an off-the-shelf single-image albedo estimation method [57] and averaging per-pixel albedo values within each semantic part. Given $\{\mathbf{A}_i\}$, we initialize albedo $\mathbf{a}(\mathbf{x})$ by minimizing the error between the projected albedo and the estimated albedo across all input images: $\min_{\mathbf{a}} \sum_i \|\pi_i(\mathbf{a}) - \mathbf{A}_i\|_2$. Here, π_i represents the perspective projection onto the image space of \mathbf{I}_i by intersecting camera rays with the surface mesh of the input scene and reading \mathbf{a} at their first intersections. We obtain semantic category labels from part IDs in synthetic scenes or using Mask2Former [3] for real scenes. Roughness and metallic are both initialized to 0.5.

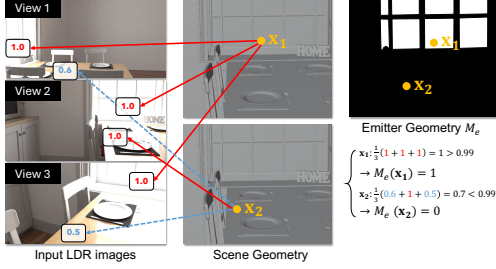


Figure 4. **Emitter geometry estimation** $M_e(\mathbf{x})$. The point \mathbf{x}_1 on the window is saturated across all input views and thus identified as an emitter. The point \mathbf{x}_2 on the table is reflective and saturated in some views (e.g., view 2) but not in others and is NOT an emitter.

5.2. HDR Emission Restoration

Given that emitters appear bright across views and produce saturated pixels in LDR images, we estimate the binary emitter geometry $M_e(\mathbf{x})$ on the surface mesh as follows:

$$M_e(\mathbf{x}) = \begin{cases} 1 & \text{if } \frac{1}{N} \sum_i v_i(\mathbf{x}) \mathbf{I}_i(\pi_i(\mathbf{x})) \geq 0.99 \\ 0 & \text{otherwise,} \end{cases} \quad (3)$$

where $v(\cdot) \in \{0, 1\}$ indicates visibility. See Figure 4.

The HDR intensity is crucial for inverse rendering but is missing in the LDR images. In order to recover the HDR lighting, we perform physically-based rendering with single-bounce path tracing to generate the images (2). To estimate the radiance at the point \mathbf{x} observed from a camera ray, we trace $N = 128$ secondary rays from \mathbf{x} , sampled with the current BRDF estimates. The resulting radiance is approximated by:

$$\mathbf{L}_r(\mathbf{x}, \boldsymbol{\omega}_o) = \sum_{i=1}^N \mathbf{L}_{\text{end}}(\mathbf{x}') f(\mathbf{x}, \boldsymbol{\omega}_i, \boldsymbol{\omega}_o), \quad (4)$$

$$\mathbf{L}_{\text{end}}(\mathbf{x}) = \begin{cases} \mathbf{L}_e(\mathbf{x}) & \text{if } M_e(\mathbf{x}) = 1 \\ \mathbf{L}_{\text{SLF}}(\mathbf{x}) & \text{otherwise,} \end{cases} \quad (5)$$

where $\mathbf{x}' = \mathbf{x} + d \cdot \boldsymbol{\omega}_i$ is the intersected point of the secondary ray along direction $\boldsymbol{\omega}_i$. Intuitively, we retrieve the radiance from the *learnable* emission radiance $\mathbf{L}_e(\mathbf{x})$ if the secondary ray hits an emitter directly, or otherwise from the pre-computed surface light field $\mathbf{L}_{\text{SLF}}(\mathbf{x})$ to approximate the global illumination. Figure 5 shows an illustration.

To recover the HDR emitter radiance, we minimize the photometric loss with gradient descent: $\min_{\mathbf{L}_e} \mathcal{L}_{\text{photo}}$, where

$$\mathcal{L}_{\text{photo}} = \sum_i \|\text{CRF}(\min(\mathbf{L}_o(\mathbf{x}, \boldsymbol{\omega}_o) \Delta t_i, 1)) - \mathbf{I}_i\|_2. \quad (6)$$

The emitter radiance $\mathbf{L}_e(\mathbf{x})$ is enhanced to match the captured images, while the BRDF and CRF are fixed in this stage. Intuitively, in order to minimize the photometric loss with physically-based rendering, the emitter intensity $\mathbf{L}_e(\mathbf{x})$ should be increased significantly and enhance the overall brightness of the rendered image. Therefore, the HDR lighting is recovered in this process.



Figure 5. **HDR emission restoration**. **Top**: Ray sampling process. Learnable direct lighting \mathbf{L}_e is retrieved if a ray hits an emitter (e.g., window) or \mathbf{L}_{SLF} is retrieved otherwise (e.g., wall). **Bottom**: HDR restoration process. By performing differentiable physically-based rendering, the photometric loss enhances the emitter intensity \mathbf{L}_e .

5.3. Shading Baking

After the HDR emission is recovered in the previous stage, we bake the diffuse and specular shading maps $\mathbf{L}_d, \mathbf{L}_s^0, \mathbf{L}_s^1$, following factorized light transport (details in supplementary material). Given a surface point intersected by a camera ray, multiple rays are sampled according to the current (fixed) BRDF. The incident radiance is computed with multi-bounce path tracing, where a ray keeps tracing if it hits a non-emissive specular surface and stops otherwise. The radiance of the endpoint follows Equation (5).

5.4. BRDF & CRF Optimization

With the baked shading maps $\mathbf{L}_d, \mathbf{L}_s^0$, and \mathbf{L}_s^1 , the albedo, metallicity, roughness, and CRF are jointly optimized. The optimization involves the following objective function:

$$\min_{\mathbf{a}, m, \sigma, \mathbf{g}} \mathcal{L}_{\text{photo}} + \lambda_a \mathcal{L}_{\text{albedo}} + \lambda_c \mathcal{L}_{\text{CRF}} + \lambda_m \mathcal{L}_{\text{mat}}, \quad (7)$$

where $\lambda_a = 0.01$, $\lambda_c = 0.001$, and $\lambda_m = 0.005$.

Photometric loss. We perform physically-based rendering, and the photometric loss $\mathcal{L}_{\text{photo}}$ is computed as in Eq. 6.

Albedo regularization. Motivated by the shift-scale-invariant loss in MonoSDF [50], we adopt a shift-invariant loss against the monocular albedo maps $\{\mathbf{A}_i\}$:

$$\mathcal{L}_{\text{albedo}} = \sum_i \|\pi_i(\mathbf{a}) - s \mathbf{A}_i\|_2, \quad (8)$$

where s is the scale used to align the two albedo maps.

CRF regularization. Base on the fair assumption that the learned CRF should not deviate from the mean curve $\bar{\mathbf{g}}$ (Eq. 1), and that the curve should be monotonically increasing, we regularize the L_2 norm of the estimated coefficients of the PCA bases, and enforce the monotonicity of the sampled CRF as follows:

$$\mathcal{L}_{\text{CRF}} = \|\mathbf{w}\|_2 + \sum_i \max(g_{i-1} - g_i, 0). \quad (9)$$

Material regularization. We apply roughness-metallicity regularization \mathcal{L}_{mat} , which enforces the consistency of surface roughness and metallic within the same semantic instances (e.g. chairs, tables). While the shading and emission are initially inaccurate and lead to erroneous BRDFs, we alternately update the BRDFs and produce better emission and shading, improving the BRDFs. Our alternating strategy yields more stable optimization and better estimation.

6. Experiments

We evaluate our method on both synthetic and real-world data and compare it against several baseline methods. We analyze the quality of our inverse rendering, relighting, and novel-view synthesis capability. Please see our supplementary material for additional results and evaluations. We will release our code and data.

Datasets. We evaluate our method and baselines on the ScanNet++ [48] and FIPT [44] datasets. ScanNet++ contains 380 real-world indoor scenes and collects multi-view LDR images with a DSLR camera at a constant exposure level. We select four scenes that cover a variety of indoor scenes (e.g., office, bathroom). The FIPT dataset consists of four synthetic and two real-world scenes. The synthetic scenes provide ground-truth geometry and material properties for evaluation. We used the LDR images provided in the dataset, where the lighting is clipped in overly-exposed regions, compressed with a nonlinear CRF, quantized into 256 levels, and stored in 8-bit PNG format. We adopt the constant exposure setting to provide a fair comparison with baselines, as they cannot handle varying exposure. We further demonstrate that IRIS handles varying exposure levels of input LDR images and estimates CRF jointly.

Baselines. We compare our method with the following baselines. *Li et al.* [25] estimate BRDF, geometry (depth & normal), and lighting condition of an indoor scene from a single image using a data-driven approach. In addition to the single image, the model also takes emitter masks as input, and we provide the mask estimated by our method (3). *NeILF* [46] targets inverse rendering from known geometry and multi-view images. The spatially-varying BRDF and illumination are parameterized as neural fields [29]. Physically-based rendering and single-bounce ray tracing are performed during the training and rendering process. The HDR-to-LDR tone mapping is modeled as a learnable gamma correction. The original FIPT [44] is designed for HDR input, and fails to estimate emission mask from LDR images. Thus, we additionally provide the emission mask estimated by our method (3). We denote this modified version as “*FIPT**”.

To further evaluate our performance, we compare the original FIPT with HDR input if the HDR information is available. This privileged information will make illumination estimation much more accurate.

Table 1. **BRDF-emission comparison on synthetic data.** Numbers are averaged across four synthetic scenes with GT [44]. The best metrics among LDR methods are highlighted in bold.

Method	Input	k_d	a' PSNR \uparrow	σ	L_e IoU \uparrow L2 \downarrow	
Li et al [25]	LDR	16.73	14.01	11.30	0.35	2.29
NeILF [46]	LDR	16.85	14.02	16.96	—	—
FIPT*	LDR	15.49	9.74	4.99	0.69	0.28
Ours	LDR	22.33	17.92	21.38	0.69	0.12
FIPT [44]	HDR	29.95	25.98	26.37	0.86	0.03

6.1. Inverse Rendering of Real Scenes

We provide a qualitative evaluation of inverse rendering in Figure 6. Conducting single-bounce ray tracing in the neural light field, NeILF [46] fails to remove the shadow in diffuse reflectance k_d , estimates lower roughness σ on the walls than the mirror, and produces an incorrect emission map. FIPT* struggles to recover surface material from LDR input, where accurate lighting information is missing. Please note that FIPT* takes emitter masks from Equation (3) as additional input, but does not recover HDR emission in the optimization procedure. On the other hand, IRIS recovers an almost shading-free diffuse field. Regarding roughness, our method effectively identifies specular surfaces with low roughness on the mirror, demonstrating better specular/rough material separation. Additionally, our proposed HDR emission estimation proves effective for real scenes, recovering HDR lighting sources (i.e., window and ceiling light). The restored HDR lighting makes the light transport more accurate and significantly enhances the performance of inverse rendering.

6.2. View Synthesis and Relighting of Real Scenes

We compare the relighting with FIPT* in Figure 7. FIPT* fails to estimate accurate surface material from LDR input and tends to recover low roughness for most surfaces, which unrealistically reflects the inserted light source and objects. To be more specific, the ground of the office (first scene) and the wall of the bathroom (second scene) look overly smooth and specular, which is not consistent with the observation and produces unreal reflections. In contrast, IRIS produces better relighting and object insertion quality thanks to better inverse rendering. The reflections on the specular surfaces (e.g., whiteboard, mirror) and the shading on the wall demonstrate the strength of IRIS for realistic relighting. Furthermore, the recovered HDR lighting can produce naturalistic specular reflection and shadows for inserted objects. Additionally, we insert moving light sources in the scene, shown in Figure 8, where the shadow on the ground and shading on the table change consistently. IRIS enables the photorealistic rendering of novel objects under diverse lighting and from arbitrary viewpoints, showcasing the significant potential for content creation applications.

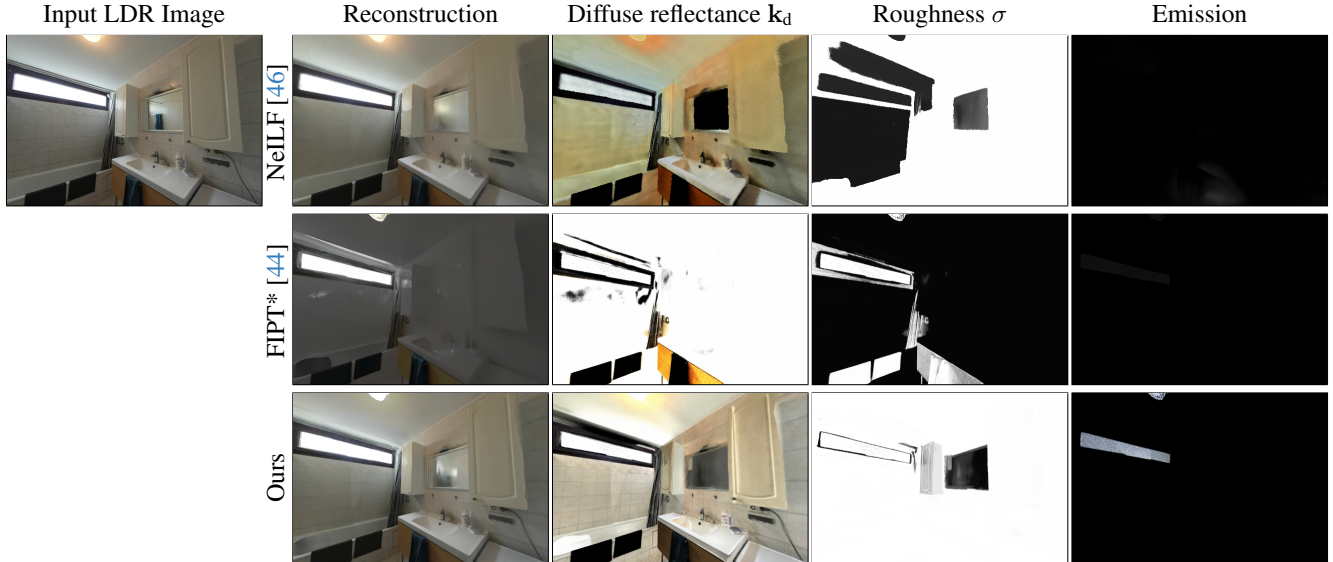


Figure 6. **Decompositions of real scenes** from the ScanNet++ [48]. In addition to good reconstruction, IRIS produces a detailed diffuse map, identifies the mirror as a low-roughness region and recovers HDR lighting from windows and ceiling light. Please note that the emission maps are normalized to visualize the relative intensity.



Figure 7. **Relighting and object insertion with real scenes** from the ScanNet++ [48] and FIPT datasets [44]. When inserting new light sources (Relighting 1 & 2), IRIS not only changes shadow but also produces reflection of the light on the whiteboard (first scene) and mirror (second scene), enhancing realism substantially. The recovered HDR lighting also strengthens the reflection and shadow of inserted objects (“Object Insertion” column).

6.3. Quantitative Evaluation

Quantitative evaluation of inverse rendering is difficult for real-world scenes as ground truth is not available. As a result, we evaluate IRIS and baselines on the synthetic scenes from FIPT, where ground truth of surface material, illumination,

and relighting are provided. Please note that we use ground truth mesh during optimization for all methods to minimize the influence of imperfect geometry and conduct a fair comparison. We compute the metrics of inverse rendering and provide the comparison in Table 1, which aggregates the

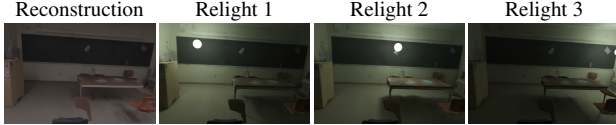


Figure 8. Relighting with a moving light ball in a real scene.

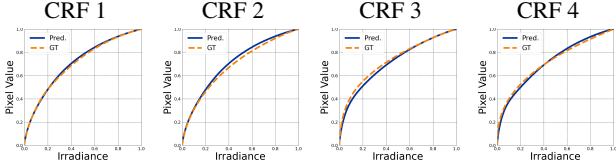


Figure 9. CRF estimation from real-world devices. The orange dashed line is the ground truth CRF, and the blue line our estimate.

results from the 4 synthetic FIPT scenes [44].

We compare the roughness σ , diffuse reflectance k_d among the diffuse surfaces, and material reflectance: a' . We report the PSNR for these BRDF estimates. For emission, we calculate the intersection over the union (IoU) of the emission masks and compare the L_2 error of estimated emission maps. All the estimates are rendered in image space and compared with ground truth.

Table 1 shows that our method surpasses all baseline methods that use LDR inputs regarding inverse rendering quality. Compared to the state-of-the-art single-view method [25], our method excels in all metrics across various scenes, indicating the superior decomposition of material properties from multi-view observations. Furthermore, even when the estimated emitter mask is provided for FIPT*, it fails to recover emission radiance, leading to compromised BRDF estimation accuracy. The L_2 error of emission maps shows that our proposed HDR restoration (Section 5.2) successfully recovers the HDR lighting from LDR observations, which leads to better light transport modeling and more accurate BRDF estimation. We also compare with FIPT taking HDR images as input (bottom row), which serves as a reference, indicating complete lighting information is crucial for inverse rendering. IRIS recovers HDR and achieves the smallest metric gaps among all methods, taking LDR input.

We compare novel-view synthesis and relighting of all competing algorithms and report results in Table 2. The novel-view synthesis (NVS) results show that IRIS is comparable with baseline methods [46], while exhibiting superior material and lighting estimation. Our main focus is relighting, and IRIS outperforms all baselines with LDR input, demonstrating the effectiveness of inverse rendering.

6.4. Ablation Study

We validate the design choices and provide an ablation study in Table 3, where we compute PSNR for material (k_d , a' , σ) and MSE for CRF curves and emission maps L_e . The emitter mask estimation in Equation (3) identifies the emitter

Table 2. Quantitative results of novel-view synthesis (NVS) and relighting on synthetic scenes with ground truth.

	Method	Input	PSNR \uparrow	SSIM \uparrow	LPIPS \downarrow
NVS	NeILF [46]	LDR	30.031	0.899	0.180
	FIPT*	LDR	15.180	0.744	0.437
	Ours	LDR	29.468	0.903	0.181
	FIPT [44]	HDR	28.760	0.902	0.186
Relighting	Li et al. [25]	LDR	22.444	0.813	0.398
	FIPT*	LDR	11.626	0.705	0.359
	Ours	LDR	22.861	0.882	0.173
	FIPT [44]	HDR	29.012	0.902	0.139

Table 3. Ablation Study. We show PSNR for the surface material k_d , a' , σ , and MSE for CRF estimation and emission map L_e .

Emitter mask M_e (Equation (3))	CRF modeling (Equation (1))	HDR restoration (Figure 5)	k_d	a' PSNR \uparrow	σ	CRF MSE \downarrow	L_e MSE \downarrow
			22.05	15.27	5.94	—	0.75
✓			15.77	8.97	5.94	—	0.45
✓	✓		21.88	14.66	6.19	5.65	0.45
✓	✓	✓	23.22	17.52	20.35	2.01	0.20

from LDR observations and improves the emission map in the second row. CRF estimation is critical for modeling HDR-to-LDR conversion and helps inverse rendering in the third row. Nevertheless, the HDR restoration (Section 5.2) plays an important role in recovering accurate light transport from the captured images. Once the HDR light is restored by our proposed approach, the material (especially roughness σ), CRF, and emission map are improved significantly. The results demonstrate the significance of each component and show that inverse rendering from casually captured LDR images benefits from our proposed framework.

6.5. CRF Estimation

To further validate the robustness of our method, we generate LDR images from FIPT’s synthetic HDR scenes using different CRFs collected from real-world devices [10]. In this evaluation, we perform inverse rendering with IRIS and plot the CRF. The results in Figure 9 show that our method can generalize to various imaging pipelines. Please refer to the supplementary details for more analysis of CRF estimation.

7. Conclusion

We presented IRIS, an inverse rendering framework for indoor scenes from casually captured LDR images. Our key innovations include HDR lighting restoration, CRF estimation, surface material estimation, and alternating optimization to recover all scene properties accurately. IRIS estimates accurate surface material, spatially varying HDR illumination, and CRF from real-world LDR images. As a result, IRIS enables photorealistic rendering under diverse lighting and from arbitrary viewpoints, showcasing the significant potential for content creation applications.

IRIS: Inverse Rendering of Indoor Scenes from Low Dynamic Range Images

Supplementary Material

Abstract

This supplementary document shows additional details of our method and more results. We refer the readers to our supplementary webpage, which shows more results that allow for easy comparisons with the baseline methods on all scenes we use.

8. Relighting and Object Insertion Results

Our method estimates accurate surface material and spatially varying HDR illumination from LDR images, enabling various applications such as relighting and object insertion. We provide the qualitative results of real-world scenes in Figure 10, Figure 11, Figure 12, Figure 15, where we sample novel camera trajectories and render the scene at different time steps. The results demonstrate effective modeling of specular reflections on smooth surfaces (like ‘mirror’ and ‘whiteboard’) upon introducing new light sources. Moreover, our method accurately simulates inter-reflections between the scene and the inserted objects, significantly elevating the realism of the object insertion. To summarize, we show that IRIS can render real-world scenes under various illumination from different viewpoints. For more interactive visualizations and comparisons, please check our supplementary webpage.

9. Additional Evaluation Results

In addition to physically-based inverse rendering techniques like FIPT, methods based on neural radiance fields (NeRF) [29] strive for scene disentanglement by representing indoor scenes’ incident radiance fields with a 5D network [46] without constraints. Recent NeRF-based approaches like I²-SDF [56], NeILF++ [53], and NeFII [43], much like FIPT, rely on pre-calculated irradiance, and focus on surface rendering to reconstruct scene materials and/or lighting. However, these methods typically account for only single-bounce light transport, leading to compromised quality in both material and lighting reconstruction. Here, we also include comparisons with NeILF [46] and I²-SDF [56] to highlight these distinctions.

The complete metrics of inverse rendering are shown in Table 4 and the complete metrics of novel view synthesis and relighting are listed in Table 5. Our method achieves comparable novel view synthesis results and outperforms other baselines for relighting. The results underscore the effectiveness of our method in accurately decomposing intrinsic elements from LDR images.

Table 4. **BRDF-emission comparison on synthetic data.** FIPT-LDR* is provided with the GT emitter mask as additional input. The best metrics among LDR methods are highlighted in bold.

Method	k_d	a'	σ	L_e		
				IoU \uparrow	L2 \downarrow	
Kitchen	Li et al [25]	15.75	12.64	10.15	0.43	1.410
	NeILF [46]	16.63	13.73	14.77	—	—
	FIPT-LDR*	15.77	8.97	5.94	0.58	0.450
	Ours	23.22	17.52	20.35	0.58	0.203
	FIPT-HDR [44]	34.34	27.05	24.55	0.88	0.010
Bedroom	Li et al [25]	18.90	15.10	11.38	0.34	2.784
	NeILF [46]	16.85	13.99	16.03	—	—
	FIPT-LDR*	18.38	9.60	5.82	0.77	0.245
	Ours	26.44	20.95	26.47	0.77	0.043
	FIPT-HDR [44]	28.98	25.86	23.53	0.92	0.004
Livingroom	Li et al [25]	16.78	14.71	11.42	0.17	3.610
	NeILF [46]	16.06	13.86	15.95	—	—
	FIPT-LDR*	11.59	8.93	4.08	0.77	0.240
	Ours	18.09	15.45	25.28	0.77	0.103
	FIPT-HDR [44]	28.42	27.47	30.44	0.95	0.005
Bathroom	Li et al [25]	15.50	13.60	12.24	0.45	1.351
	NeILF [46]	17.85	14.49	21.09	—	—
	FIPT-LDR*	16.21	11.46	4.12	0.62	0.187
	Ours	21.56	17.74	13.43	0.62	0.135
	FIPT-HDR [44]	28.06	23.54	26.97	0.68	0.080

10. Qualitative Results of Synthetic Scenes

To verify the effectiveness of inverse rendering, we compare IRIS with several baselines on synthetic scenes provided by FIPT [44], which provide ground truth geometry, material properties, and lighting. Figure 13 shows the qualitative results of inverse rendering, including image reconstruction, material reflectance a' , roughness σ , and emission maps. While NeILF [46] achieves accurate rendering, it bakes significant shading effects into its diffuse albedo map. Li et al. [25] generate a noisy BRDF from a single image input. FIPT* tends to underestimate illumination intensity, overestimating the reflectance a' as compensation. In contrast, our method successfully recovers high-quality HDR emission from LDR input, resulting in precise intrinsic decomposition.

11. Additional Ablation Study

We visualize the CRFs with different CRF modeling techniques in Figure 17, corresponding to Table 6. The results show that from input images captured with varying exposure, our method can recover ground truth CRF, demonstrating the effectiveness and importance of CRF modeling. We parametrize the CRF as a continuous and monotonically increasing function across the domain (0, 1), and sample 1024

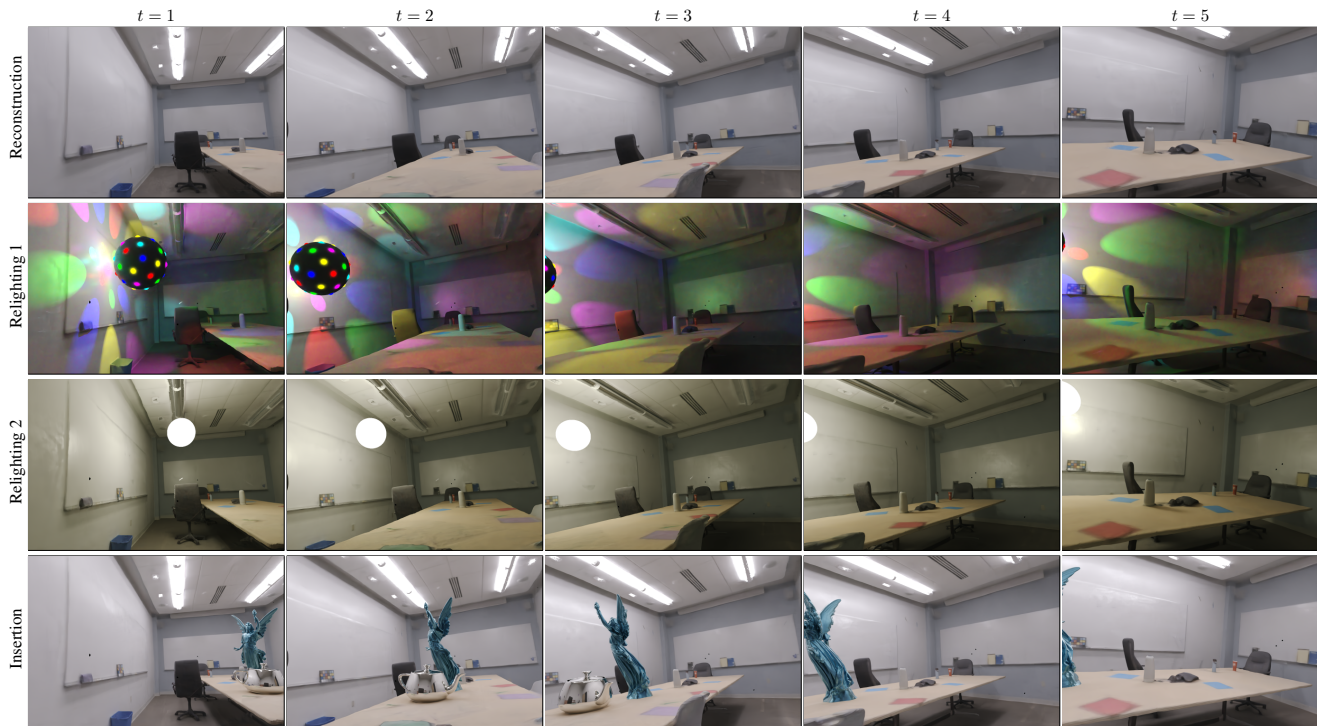


Figure 10. **Relighting and object insertion in ‘conference room’.** The inserted new light sources are reflected on the whiteboard surface, demonstrating the accuracy of the material estimation of IRIS.

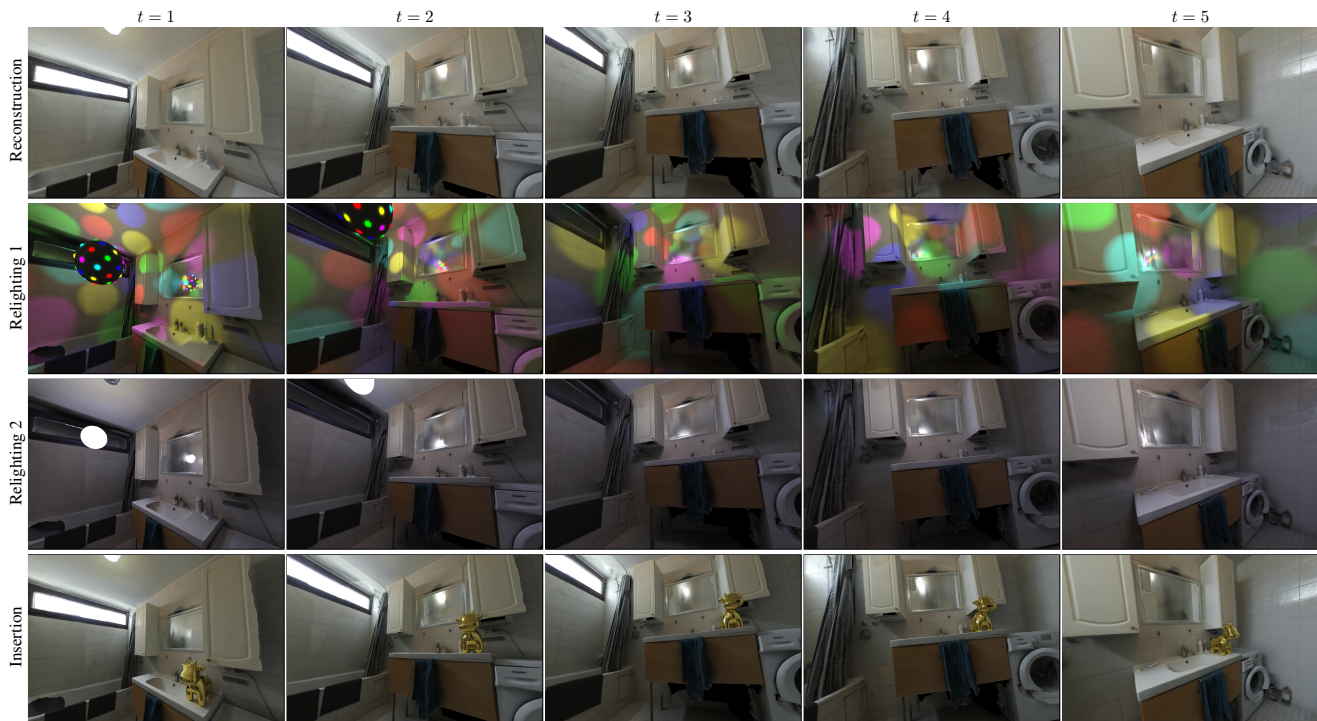


Figure 11. **Relighting and object insertion in ‘bathroom’.** The mirror is estimated as a low-roughness surface, and it reflects the new light sources and enhances the realism of relighting significantly. The inserted object also exhibits reflection of HDR lighting recovered by IRIS.

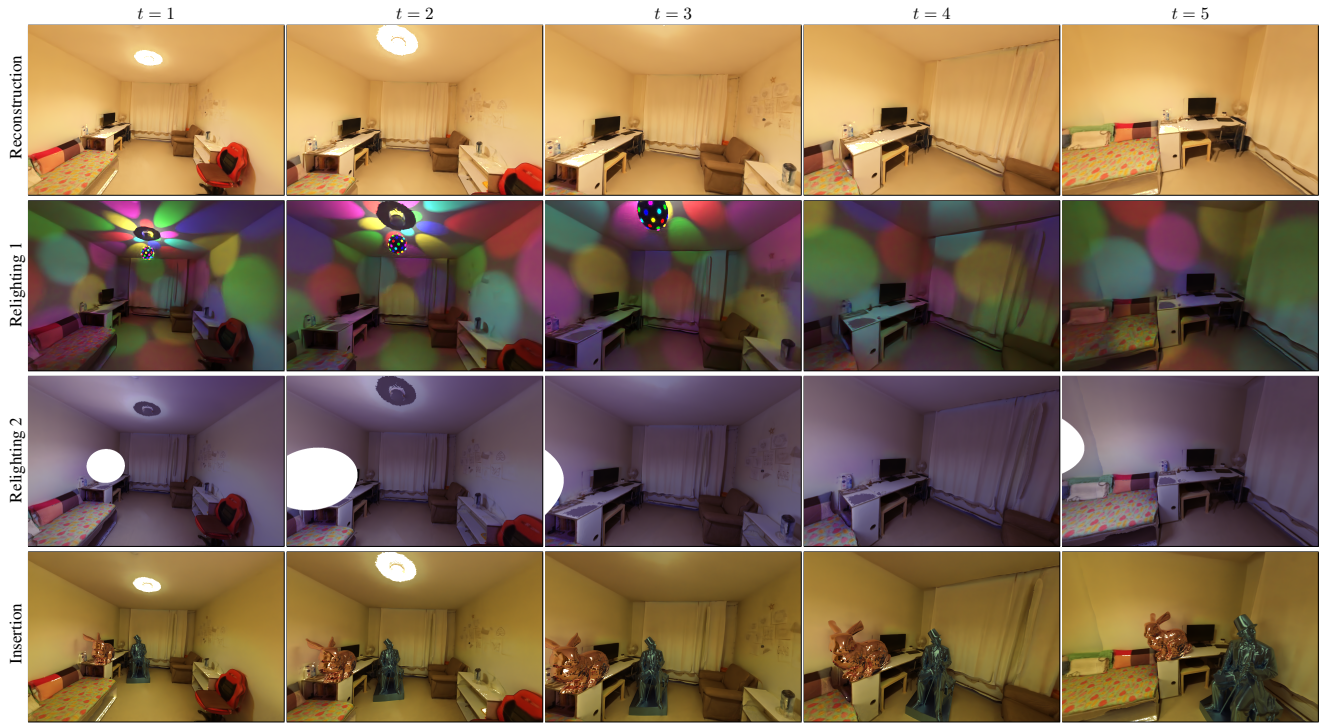


Figure 12. **Relighting and object insertion in ‘bedroom’.** The Disco ball rotates and casts colorful lights in different directions, creating realistic relighting results in the real-world scene.

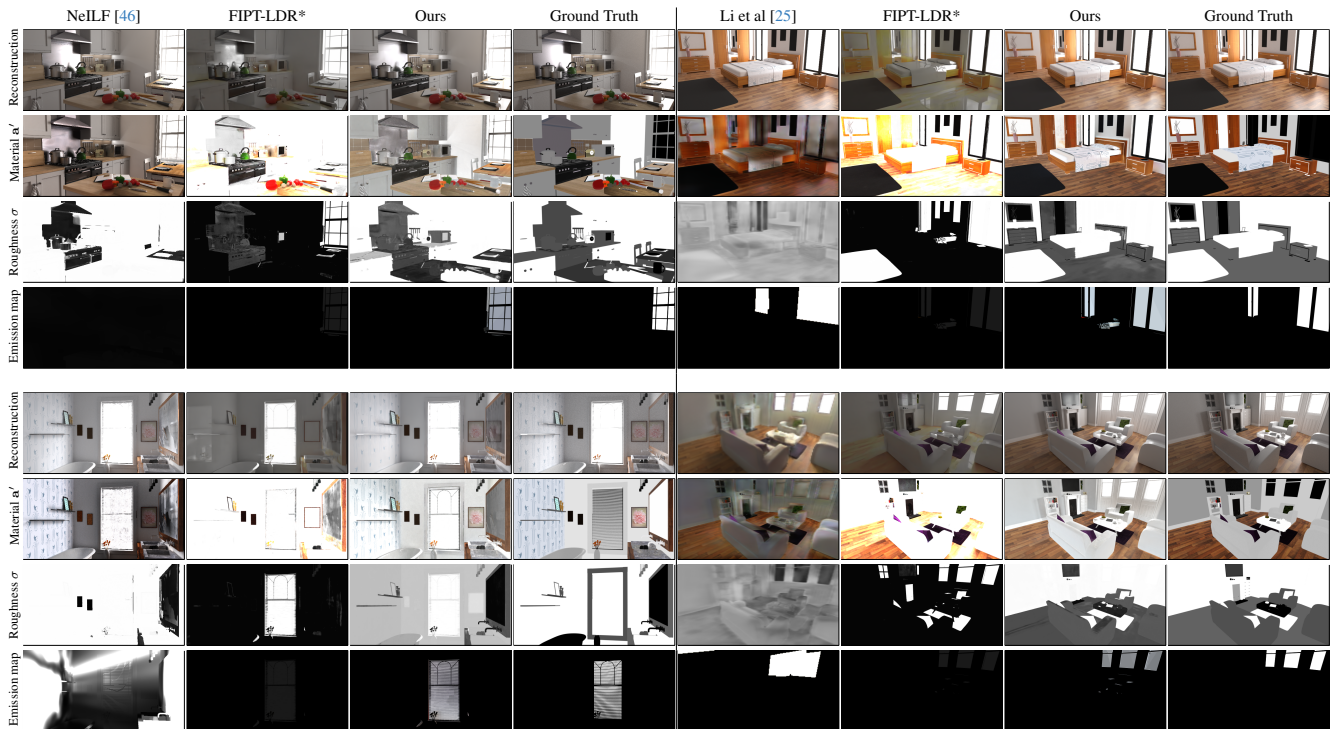


Figure 13. **Intrinsic decomposition of synthetic scenes [44].** From top to bottom, we show reconstruction, material reflectance a' , roughness σ , and emission maps. For the emission map, we show normalized HDR emission, such that it is not saturated and differences become visible. With LDR images as input, IRIS successfully recovers the HDR lighting and accurate surface material.

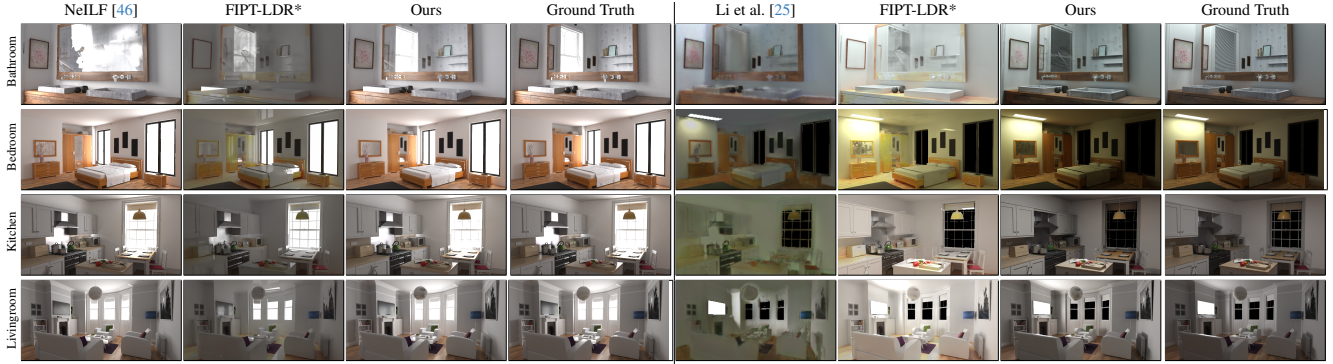


Figure 14. **Novel-view synthesis and relighting results on synthetic scenes [44].** The novel view synthesis results are shown in the left four columns, and the relighting of the same novel view are shown in the right four columns.

Table 5. **Complete quantitative results of novel view synthesis and relighting on synthetic scenes**

Method	Kitchen			Bedroom			Livingroom			Bathroom			
	PSNR \uparrow	SSIM \uparrow	LPIPS \downarrow	PSNR \uparrow	SSIM \uparrow	LPIPS \downarrow	PSNR \uparrow	SSIM \uparrow	LPIPS \downarrow	PSNR \uparrow	SSIM \uparrow	LPIPS \downarrow	
NVS	NeILF [46]	29.309	0.910	0.187	29.651	0.944	0.095	34.653	0.959	0.099	26.509	0.783	0.339
	\hat{I}^2 -SDF [56]	24.993	0.898	0.234	25.845	0.916	0.150	27.955	0.962	0.091	24.967	0.698	0.483
	FIPT-LDR*	16.372	0.776	0.381	14.536	0.784	0.389	16.146	0.805	0.361	13.665	0.609	0.616
	Ours	29.730	0.916	0.192	28.765	0.940	0.094	31.368	0.954	0.104	28.008	0.802	0.335
FIPT-HDR [44]	29.059	0.924	0.180	27.670	0.940	0.095	28.524	0.951	0.109	29.788	0.792	0.358	
Relight	Li22 [25]	21.755	0.815	0.381	23.662	0.851	0.342	21.631	0.841	0.395	22.887	0.747	0.475
	FIPT-LDR*	11.932	0.715	0.283	13.132	0.701	0.334	9.198	0.710	0.345	12.240	0.694	0.473
	Ours	23.818	0.873	0.143	25.483	0.892	0.166	18.478	0.906	0.127	23.664	0.856	0.254
	FIPT-HDR [44]	27.597	0.886	0.115	28.411	0.878	0.155	32.543	0.964	0.078	27.497	0.881	0.208



Figure 15. **Relighting and object insertion in kitchen.** From top to bottom, we visualize the reconstruction (1st row), relighting (2nd), and object insertion (3rd).



Figure 16. **Visualizing albedo a during the training.** We show that leveraging data-driven IRISformer [57] estimation (left) provides us good albedo initialization (center), and final result is refined with physically-based rendering model.

Table 6. **Ablation of CRF modeling.**

Method	k_d	PSNR \uparrow		$L_2 \downarrow$
		a'	σ	CRF
Constant exposure	24.24	19.11	27.42	4.074
Mean CRF \bar{g}	23.61	19.55	15.25	4.240
Gamma 1/2.2	23.65	20.05	15.72	3.683
Full model	26.82	23.43	26.63	1.363

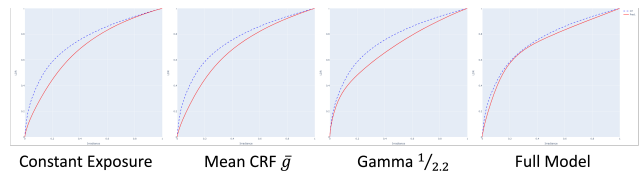


Figure 17. **CRF comparison visualization.** The blue dash lines are the ground-truth CRF, and the red lines are the estimated CRF after the optimization. We compare with three variants of CRF modeling settings. We show that the full model with varying exposure and learnable CRF model can approximate the ground truth quite well.

points between 0 and 1 and calculate the L2 distance between the function values and the ground truth. We compare with three CRF alternatives: (1) constant exposure input, (2) Mean CRF \bar{g} (the mean CRF from 201 empirical CRF functions measured in the real world [11]), and (3) Gamma 1/2.2 ($g(x) = x^{1/2.2}$, as used in FIPT [44]). Our method outperforms the single exposure approach, suggesting the benefits of using varying exposure values to enhance dynamic range. It also achieves better results than constant CRF functions, justifying joint CRF optimization’s merits.

To validate the design choices of our method, we conducted an ablation study of loss terms, the results of which are compared in terms of inverse rendering quality in Table 8. This evaluation was carried out on four synthetic scenes, with the report focusing on the average metric across these scenes. Without the CRF regularization term \mathcal{L}_{CRF} , the CRF curve could appear highly unnatural. This aberration might not be evident in the photometric loss, as albedo and emission could be inaccurately adjusted to minimize this loss. Without the albedo regularization term $\mathcal{L}_{\text{albedo}}$, the ambiguity between lighting and material leads to less accurate roughness and CRF estimation. Our method, with the inclusion of regularization terms, achieves the best CRF estimation when both $\mathcal{L}_{\text{albedo}}$ and \mathcal{L}_{CRF} are implemented. Additionally, we depict the evolution of albedo at different stages of the process in Figure 16, demonstrating the improvement in the quality of albedo generated by our method throughout the optimization.

12. Factorized Light Transport

We follow the rendering equation [16] to model physically-based light transport for realistic rendering:

$$\mathbf{L}_o(\mathbf{x}, \boldsymbol{\omega}_o) = \mathbf{L}_e(\mathbf{x}, \boldsymbol{\omega}_o) + \int_{\Omega^+} \mathbf{L}_i(\mathbf{x}, \boldsymbol{\omega}_i) f(\mathbf{x}, \boldsymbol{\omega}_i, \boldsymbol{\omega}_o) d\boldsymbol{\omega}_i,$$

where \mathbf{L}_o is the radiance observed along a ray $(\mathbf{x}, \boldsymbol{\omega}_o)$ for a 3D position \mathbf{x} and a direction $\boldsymbol{\omega}_o$, \mathbf{L}_e is the emission term, $\mathbf{L}_r = \int_{\Omega^+} \mathbf{L}_i(\mathbf{x}, \boldsymbol{\omega}_i) f(\mathbf{x}, \boldsymbol{\omega}_i, \boldsymbol{\omega}_o) d\boldsymbol{\omega}_i$ is the reflectance term, and $f(\mathbf{x}, \boldsymbol{\omega}_i, \boldsymbol{\omega}_o)$ is the BRDF. While \mathbf{L}_i encapsulates recursive incident radiance computation, we represent spatially-varying materials using the Cook-Torrance BRDF [4]:

$$f(\mathbf{x}, \boldsymbol{\omega}_i, \boldsymbol{\omega}_o) = \frac{\mathbf{k}_d(\mathbf{x})}{\pi} (\mathbf{n} \cdot \boldsymbol{\omega}_i)_+ + \frac{F \cdot D \cdot G}{4(\mathbf{n} \cdot \boldsymbol{\omega}_o)}, \quad (10)$$

where $D(\mathbf{h}, \mathbf{n}, \sigma(\mathbf{x}))$ describes the distribution of microfacet orientations, $G(\boldsymbol{\omega}_i, \boldsymbol{\omega}_o, \mathbf{n}, \sigma(\mathbf{x}))$ encodes the masking and shadowing effects between microfacets, and $F(\boldsymbol{\omega}_i, \mathbf{h}, \mathbf{k}_s(\mathbf{x}))$ is the Fresnel reflection term. The recursive integral in Equation (2) is computationally expensive and usually approximated with Monte-Carlo path tracing [16, 18] with multiple bounces. The rendering equation can be accelerated by factorizing the BRDF term from the integral [17, 37, 41]:

$$\mathbf{L}_r(\mathbf{x}, \boldsymbol{\omega}_o) = \mathbf{k}_d \mathbf{L}_d(\mathbf{x}) + \mathbf{k}_s \mathbf{L}_s^0(\mathbf{x}, \boldsymbol{\omega}_o, \sigma) + \mathbf{L}_s^1(\mathbf{x}, \boldsymbol{\omega}_o, \sigma), \quad (11)$$

Table 7. Notation table.

Symbol	Description
$(\cdot)_+$	dot product clamped to positive value
$\boldsymbol{\omega}_i$	incident light direction
$\boldsymbol{\omega}_o$	outgoing light direction
\mathbf{h}	half vector $(\boldsymbol{\omega}_i + \boldsymbol{\omega}_o) / \ \boldsymbol{\omega}_i + \boldsymbol{\omega}_o\ _2$
\mathbf{n}	surface normal
\mathbf{x}	3D position
$\mathbf{a}(\mathbf{x})$	surface albedo (base color)
$m(\mathbf{x})$	surface metallicness
$\sigma(\mathbf{x})$	surface roughness
$\mathbf{k}_d(\mathbf{x})$	diffuse reflectivity $\mathbf{a}(\mathbf{x})(1 - m(\mathbf{x}))$
$\mathbf{k}_s(\mathbf{x})$	specular reflectivity $\mathbf{a}(\mathbf{x})m(\mathbf{x}) + 0.04(1 - m(\mathbf{x}))$
$D(\cdot)$	GGX normal distribution
$F(\cdot)$	Schlick’s approximation of Fresnel coefficients
$G(\cdot)$	Geometry (shadow-masking) term

where we decompose the reflectance term into a diffuse shading term $\mathbf{L}_d(\mathbf{x}) = \int_{\Omega^+} \mathbf{L}_i(\mathbf{x}, \boldsymbol{\omega}_i) \frac{(\mathbf{n} \cdot \boldsymbol{\omega}_i)_+}{\pi} d\boldsymbol{\omega}_i$, as well as two specular terms

$$\mathbf{L}_s^0(\mathbf{x}, \boldsymbol{\omega}_o, \sigma) = \int_{\Omega^+} \mathbf{L}_i(\mathbf{x}, \boldsymbol{\omega}_i) \frac{F_0 D G}{4(\mathbf{n} \cdot \boldsymbol{\omega}_o)} d\boldsymbol{\omega}_i, \quad (12)$$

$$\mathbf{L}_s^1(\mathbf{x}, \boldsymbol{\omega}_o, \sigma) = \int_{\Omega^+} \mathbf{L}_i(\mathbf{x}, \boldsymbol{\omega}_i) \frac{F_1 D G}{4(\mathbf{n} \cdot \boldsymbol{\omega}_o)} d\boldsymbol{\omega}_i, \quad (13)$$

where $F_0 = 1 - F_1$ and $F_1 = (1 - \mathbf{h} \cdot \boldsymbol{\omega}_i)^5$. $\mathbf{k}_d(\mathbf{x})$ is diffuse reflectance and $\mathbf{k}_s(\mathbf{x})$ is specular reflectance calculated from the BRDF. \mathbf{L}_s^* is further approximated by linearly interpolating the shading maps pre-computed at various roughness σ levels: $\mathbf{L}_s^*(\cdot, \sigma) = \text{LERP}(\{\mathbf{L}_s^*(\cdot, \sigma_i)\}_{i=1}^6, \sigma)$, where $\{\sigma_i\}_{i=1}^6$ is uniformly sampled between (0, 1). With the factorization formulation, the shading maps $\mathbf{L}_d, \{\mathbf{L}_s^0(\cdot, \sigma_i), \mathbf{L}_s^1(\cdot, \sigma_i)\}_{i=1}^6$ can be pre-computed and allow for more efficient and stable optimization of material properties and HDR lighting.

13. Implementation Details

To clarify the equations in the paper, we describe the mathematical expressions and associated physical meanings in Table 7.

Varying exposure data generation. In real-world photography pipelines, exposure levels are adjusted by manipulating camera settings, such as shutter speed, aperture size, and ISO, to capture bright and dark regions. While the FIPT dataset [44] assumes single exposure and utilizes a simplistic camera response function (CRF) model defined as $\text{CRF}(x) = x^{1/2.2}$, our approach simulates a capturing process that is both more realistic and challenging. To create LDR images of synthetic scenes for CRF metric calculation, we split the HDR images of the same scene into five exposure levels $\{\Delta t_i\}_{i=1}^5$, s.t. $\Delta t_i < \Delta t_{i+1}$, where the brightest HDR image corresponds to Δt_0 , and conversely, the darkest

Table 8. Ablation study of loss terms in optimization.

Method	k_d	PSNR \uparrow		L_2 \downarrow
		\mathbf{a}'	σ	CRF
$-\mathcal{L}_{\text{CRF}}$	20.085	17.836	23.958	6.100
$-\mathcal{L}_{\text{albedo}}$	24.005	20.350	15.425	1.969
Full model	23.839	20.082	17.518	1.872

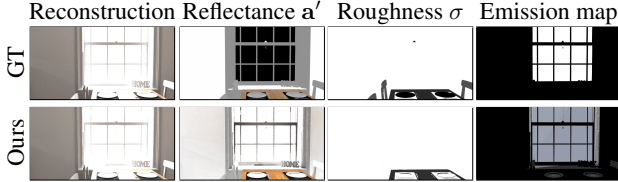


Figure 18. Failure cases.

to Δt_5 , effectively mimicking an auto-exposure mechanism. Subsequently, we apply each exposure level to the HDR image and convert it into LDR format with the CRF derived from real-world sensors [11].

Direct illumination $L_e(\mathbf{x})$. We first identify the mesh faces $\{f_i\}$ of emitters with the emitter mask $M_e(\mathbf{x})$ defined on the mesh faces. We associate a learnable 3-dimensional parameter for each face: $\mathbf{e}(f) \in \mathbb{R}^3$, representing the emitted light radiance. These parameters are then optimized during the HDR emission restoration phase.

BRDF. The surface material is represented as a neural field: $(\mathbf{a}, m, \sigma) = \mathbf{F}(\mathbf{x})$, the model architecture of which is based on Instant-NGP [31].

Shading Baking. Intuitively, the ray tracing continues if it encounters a non-emissive, specular surface (identified by a roughness threshold of 0.6), and stops otherwise. The radiance at the endpoint adheres to Eq. 11 in the main paper. The view-independent term $L_{\text{SLF}}(\mathbf{x})$ effectively approximates the global illumination on diffuse surfaces, which also expedites the rendering process. This is because rays typically reach diffuse surfaces within a few bounces, eliminating the need for further path tracing.

$$L_i(\mathbf{x}, \boldsymbol{\omega}) = L_{\text{end}}(\mathbf{x}_n) \prod_{i=1}^{n-1} f(\mathbf{x}_{i+1} \rightarrow \mathbf{x}_i) \quad (14)$$

s.t. $\sigma(\mathbf{x}_i) \leq 0.6, M_e(\mathbf{x}_i) = 0, \forall i < n,$

where $\{\mathbf{x}_i\}_{i=1}^n$ are the intersected points along the paths.

14. Limitations

Our emitter mask estimation may be inaccurate especially when images are largely saturated. An incorrect mask cannot

be recovered from as masks are not further optimized. Our CRF model is global and it cannot capture complex non-local tone-mapping or white-balance changes. Addressing these issues would allow for a truly practical method for inverse rendering and is left for future work.

References

- [1] Dejan Azinovic, Tzu-Mao Li, Anton Kaplanyan, and Matthias Nießner. Inverse path tracing for joint material and lighting estimation. In *CVPR*, 2019. 2, 4
- [2] Sai Bi, Zexiang Xu, Pratul Srinivasan, Ben Mildenhall, Kalyan Sunkavalli, Miloš Hašan, Yannick Hold-Geoffroy, David Kriegman, and Ravi Ramamoorthi. Neural reflectance fields for appearance acquisition. [arXiv:2008.03824](https://arxiv.org/abs/2008.03824), 2020. 2
- [3] Bowen Cheng, Ishan Misra, Alexander G. Schwing, Alexander Kirillov, and Rohit Girdhar. Masked-attention mask transformer for universal image segmentation. In *CVPR*, 2022. 4
- [4] Robert L Cook and Kenneth E. Torrance. A reflectance model for computer graphics. *ACM Transactions on Graphics (ToG)*, 1982. 3, 13
- [5] Paul E. Debevec and Jitendra Malik. Recovering high dynamic range radiance maps from photographs. In *SIGGRAPH*, 1997. 3
- [6] Valentin Deschaintre, Miika Aittala, Fredo Durand, George Drettakis, and Adrien Bousseau. Single-image SVBRDF capture with a rendering-aware deep network. *ACM Transactions on Graphics (ToG)*, 37(4):128:1–15, 2018. 2
- [7] Ainaz Eftekhari, Alexander Sax, Jitendra Malik, and Amir Zamir. Omnidata: A scalable pipeline for making multi-task mid-level vision datasets from 3D scans. In *ICCV*, 2021. 4
- [8] Marc-André Gardner, Kalyan Sunkavalli, Ersin Yumer, Xiaohui Shen, Emiliano Gambaretto, Christian Gagné, and Jean-François Lalonde. Learning to predict indoor illumination from a single image. *ACM Transactions on Graphics*, 36(6):176:1–14, 2017. 2
- [9] Dan B Goldman, Brian Curless, Aaron Hertzmann, and Steven M Seitz. Shape and spatially-varying BRDFs from photometric stereo. *IEEE Transactions on Pattern Analysis and Machine Intelligence*, 32(6):1060–1071, 2009. 2
- [10] Michael D Grossberg and Shree K Nayar. What is the space of camera response functions? In *CVPR*, 2003. 8
- [11] Michael D. Grossberg and Shree K. Nayar. Modeling the space of camera response functions. *IEEE TPAMI*, 26(10):1272–1282, 2004. 3, 13, 14
- [12] Jon Hasselgren, Nikolai Hofmann, and Jacob Munkberg. Shape, light & material decomposition from images using monte carlo rendering and denoising. *NeurIPS*, 2022. 2

- [13] Xin Huang, Qi Zhang, Ying Feng, Hongdong Li, Xuan Wang, and Qing Wang. HDR-NeRF: High dynamic range neural radiance fields. In *CVPR*, 2022. 3
- [14] Wenzel Jakob, Sébastien Speierer, Nicolas Roussel, Merlin Nimier-David, Delio Vicini, Tizian Zeltner, Baptiste Nicolet, Miguel Crespo, Vincent Leroy, and Ziyi Zhang. Mitsuba 3 renderer, 2022. <https://mitsuba-renderer.org>. 2
- [15] Haiyan Jin, Isabella Liu, Peijia Xu, Xiaoshuai Zhang, Songfang Han, Sai Bi, Xiaowei Zhou, Zexiang Xu, and Hao Su. TensoIR: Tensorial inverse rendering. *CVPR*, 2023. 2, 3
- [16] James T Kajiya. The rendering equation. In *SIG-GRAPH*, 1986. 4, 13
- [17] Jaroslav Krivánek and Pascal Gautron. *Practical global illumination with irradiance caching*. Springer, 2022. 4, 13
- [18] Eric Lafortune. *Mathematical models and Monte Carlo algorithms for physically based rendering*. PhD thesis, Katholieke Universiteit Leuven, 1996. 4, 13
- [19] Xiao Li, Yue Dong, Pieter Peers, and Xin Tong. Modeling surface appearance from a single photograph using self-augmented convolutional neural networks. *ACM Transactions on Graphics (ToG)*, 36(4):45:1–11, 2017. 2
- [20] Zhengqi Li and Noah Snavely. CGIntrinsics: Better intrinsic image decomposition through physically-based rendering. In *ECCV*, 2018. 2
- [21] Zhengqi Li and Noah Snavely. Learning intrinsic image decomposition from watching the world. In *CVPR*, 2018. 2
- [22] Zhengqin Li, Kalyan Sunkavalli, and Manmohan Chandraker. Materials for masses: SVBRDF acquisition with a single mobile phone image. In *ECCV*, 2018. 2
- [23] Zhengqin Li, Mohammad Shafiei, Ravi Ramamoorthi, Kalyan Sunkavalli, and Manmohan Chandraker. Inverse rendering for complex indoor scenes: Shape, spatially-varying lighting and svbrdf from a single image. In *CVPR*, 2020. 2
- [24] Zhengqin Li, Ting-Wei Yu, Shen Sang, Sarah Wang, Meng Song, Yuhan Liu, Yu-Ying Yeh, Rui Zhu, Nitesh Gundavarapu, Jia Shi, et al. OpenRooms: An open framework for photorealistic indoor scene datasets. In *CVPR*, 2021. 2
- [25] Zhengqin Li, Jia Shi, Sai Bi, Rui Zhu, Kalyan Sunkavalli, Miloš Hašan, Zexiang Xu, Ravi Ramamoorthi, and Manmohan Chandraker. Physically-based editing of indoor scene lighting from a single image. In *ECCV*, 2022. 2, 6, 8, 9, 11, 12
- [26] Zhi-Hao Lin, Bohan Liu, Yi-Ting Chen, David Forsyth, Jia-Bin Huang, Anand Bhattad, and Shenlong Wang. UrbanIR: Large-scale urban scene inverse rendering from a single video. *3DV*, 2025. 2
- [27] Yu-Lun Liu, Wei-Sheng Lai, Yu-Sheng Chen, Yi-Lung Kao, Ming-Hsuan Yang, Yung-Yu Chuang, and Jia-Bin Huang. Single-image HDR reconstruction by learning to reverse the camera pipeline. In *CVPR*, 2020. 3
- [28] Demetris Marnerides, Thomas Bashford-Rogers, Jonathan Hatchett, and Kurt Debattista. ExpandNet: A deep convolutional neural network for high dynamic range expansion from low dynamic range content. *Computer Graphics Forum*, 2018. 3
- [29] Ben Mildenhall, Pratul P. Srinivasan, Matthew Tancik, Jonathan T. Barron, Ravi Ramamoorthi, and Ren Ng. NeRF: Representing scenes as neural radiance fields for view synthesis. In *ECCV*, 2020. 6, 9
- [30] Ben Mildenhall, Peter Hedman, Ricardo Martin-Brualla, Pratul Srinivasan, and Jonathan T. Barron. NeRF in the dark: High dynamic range view synthesis from noisy raw images. In *CVPR*, 2022. 3
- [31] Thomas Müller, Alex Evans, Christoph Schied, and Alexander Keller. Instant neural graphics primitives with a multiresolution hash encoding. *ACM TOG*, 2022. 3, 14
- [32] Jacob Munkberg, Jon Hasselgren, Tianchang Shen, Jun Gao, Wenzheng Chen, Alex Evans, Thomas Müller, and Sanja Fidler. Extracting triangular 3D models, materials, and lighting from images. In *CVPR*, 2022. 2
- [33] Merlin Nimier-David, Zhao Dong, Wenzel Jakob, and Anton Kaplanyan. Material and lighting reconstruction for complex indoor scenes with texture-space differentiable rendering. In *Eurographics Symposium on Rendering*, 2021. 2, 4
- [34] Julien Philip, Sébastien Morgenthaler, Michaël Gharbi, and George Drettakis. Free-viewpoint indoor neural relighting from multi-view stereo. *ACM Trans. Graph.*, 40(5):194:1–18, 2021. 2
- [35] Erik Reinhard, Greg Ward, Sumanta Pattanaik, Paul Debevec, Wolfgang Heidrich, and Karol Myszkowski. *High Dynamic Range Imaging – Acquisition, Display and Image-Based Lighting*. Morgan Kaufmann, 2nd edition, 2010. 1
- [36] Mike Roberts, Jason Ramapuram, Anurag Ranjan, Atulit Kumar, Miguel Angel Bautista, Nathan Paczan, Russ Webb, and Joshua M. Susskind. Hypersim: A photorealistic synthetic dataset for holistic indoor scene understanding. In *ICCV*, 2021. 2
- [37] Dario Seyb, Peter-Pike Sloan, Ari Silvennoinen, Michał Iwanicki, and Wojciech Jarosz. The design and evolution of the UberBake light baking system. *ACM Transactions on Graphics (TOG)*, 2020. 4, 13
- [38] Pratul P Srinivasan, Ben Mildenhall, Matthew Tancik, Jonathan T Barron, Richard Tucker, and Noah Snavely. Lighthouse: Predicting lighting volumes for spatially-coherent illumination. In *CVPR*, 2020. 2

- [39] Pratul P. Srinivasan, Boyang Deng, Xiuming Zhang, Matthew Tancik, Ben Mildenhall, and Jonathan T. Barron. NeRV: Neural reflectance and visibility fields for relighting and view synthesis. In *CVPR*, 2021. 3
- [40] Cheng Sun, Guangyan Cai, Zhengqin Li, Kai Yan, Cheng Zhang, Carl Marshall, Jia-Bin Huang, Shuang Zhao, and Zhao Dong. Neural-pbir reconstruction of shape, material, and illumination. In *ICCV*, 2023. 2
- [41] Zian Wang, Jonah Philion, Sanja Fidler, and Jan Kautz. Learning indoor inverse rendering with 3D spatially-varying lighting. In *ICCV*, 2021. 4, 13
- [42] Zian Wang, Tianchang Shen, Jun Gao, Shengyu Huang, Jacob Munkberg, Jon Hasselgren, Zan Gojcic, Wenzheng Chen, and Sanja Fidler. Neural fields meet explicit geometric representations for inverse rendering of urban scenes. In *CVPR*, 2023. 2, 3
- [43] Haoqian Wu, Zhipeng Hu, Lincheng Li, Yongqiang Zhang, Changjie Fan, and Xin Yu. NeFII: Inverse rendering for reflectance decomposition with near-field indirect illumination. In *CVPR*, 2023. 9
- [44] Liwen Wu, Rui Zhu, Mustafa B Yaldiz, Yin hao Zhu, Hong Cai, Janarбек Matai, Fatih Porikli, Tzu-Mao Li, Manmohan Chandraker, and Ravi Ramamoorthi. Factorized inverse path tracing for efficient and accurate material-lighting estimation. In *ICCV*, 2023. 2, 3, 4, 6, 7, 8, 9, 11, 12, 13
- [45] Xin Yang, Ke Xu, Yibing Song, Qiang Zhang, Xiaopeng Wei, and Rynson WH Lau. Image correction via deep reciprocating HDR transformation. In *CVPR*, 2018. 3
- [46] Yao Yao, Jingyang Zhang, Jingbo Liu, Yihang Qu, Tian Fang, David McKinnon, Yanghai Tsin, and Long Quan. NeILF: Neural incident light field for physically-based material estimation. In *ECCV*, 2022. 2, 6, 7, 8, 9, 11, 12
- [47] Lior Yariv, Peter Hedman, Christian Reiser, Dor Verbin, Pratul P Srinivasan, Richard Szeliski, Jonathan T Barron, and Ben Mildenhall. Baked sdf: Meshing neural sdfs for real-time view synthesis. In *ACM SIGGRAPH computer graphics*, 2023. 4
- [48] Chandan Yeshwanth, Yueh-Cheng Liu, Matthias Nießner, and Angela Dai. ScanNet++: A high-fidelity dataset of 3D indoor scenes. In *ICCV*, 2023. 6, 7
- [49] Bohan Yu, Siqi Yang, Xuanning Cui, Siyan Dong, Baoquan Chen, and Boxin Shi. MILO: Multi-bounce inverse rendering for indoor scene with light-emitting objects. *IEEE TPAMI*, 2023. 2, 4
- [50] Zehao Yu, Songyou Peng, Michael Niemeyer, Torsten Sattler, and Andreas Geiger. MonoSDF: Exploring monocular geometric cues for neural implicit surface reconstruction. In *NeurIPS*, 2022. 4, 5
- [51] Zheng Zeng, Valentin Deschaintre, Iliyan Georgiev, Yannick Hold-Geoffroy, Yiwei Hu, Fujun Luan, Ling-Qi Yan, and Miloš Hašan. RGB \leftrightarrow X: Image decomposition and synthesis using material- and lighting-aware diffusion models. In *SIGGRAPH*, 2024. 2
- [52] Jinsong Zhang and Jean-François Lalonde. Learning high dynamic range from outdoor panoramas. In *ICCV*, 2017. 3
- [53] Jingyang Zhang, Yao Yao, Shiwei Li, Jingbo Liu, Tian Fang, David McKinnon, Yanghai Tsin, and Long Quan. NeILF++: Inter-reflectable light fields for geometry and material estimation. In *ICCV*, 2023. 2, 3, 9
- [54] Kai Zhang, Fujun Luan, Qianqian Wang, Kavita Bala, and Noah Snavely. PhysSG: Inverse rendering with spherical Gaussians for physics-based material editing and relighting. In *CVPR*, 2021. 2, 3
- [55] Xiuming Zhang, Pratul P Srinivasan, Boyang Deng, Paul Debevec, William T Freeman, and Jonathan T Barron. NeRFactor: Neural factorization of shape and reflectance under an unknown illumination. *ACM TOG*, 2021. 2
- [56] Jingsen Zhu, Yuchi Huo, Qi Ye, Fujun Luan, Jifan Li, Dianbing Xi, Lisha Wang, Rui Tang, Wei Hua, Hujun Bao, and Rui Wang. I²-SDF: Intrinsic indoor scene reconstruction and editing via raytracing in neural SDFs. In *CVPR*, 2023. 2, 4, 9, 12
- [57] Rui Zhu, Zhengqin Li, Janarбек Matai, Fatih Porikli, and Manmohan Chandraker. IRISformer: Dense vision transformers for single-image inverse rendering in indoor scenes. In *CVPR*, 2022. 2, 4, 12